Journal of Alloys and Compounds 920 (2022) 165912

Contents lists available at ScienceDirect

Journal of Alloys and Compounds

journal homepage: www.elsevier.com/locate/jalcom

Ultra-broadband near-infrared $Gd_3MgScGa_2SiO_{12}$: Cr, Yb phosphors: Photoluminescence properties and LED applications

Lipeng Jiang[a], Xue Jiang[a], Jihuan Xie[b], Haiying Sun[b], Liangliang Zhang[c], Xiuling Liu[b], Zhaohui Bai[b], Guocai Lv[d], Yanjing Su[a,*]

[a] Beijing Advanced Innovation Center for Materials Genome Engineering, Corrosion and Protection Center, University of Science and Technology Beijing, Beijing 100083, China
[b] School of Materials Science and Engineering, Changchun University of Science and Technology, Changchun 130022, China
[c] State Key Laboratory of Luminescence and Applications, Changchun Institute of Optics, Fine Mechanics and Physics, Chinese Academy of Sciences, 3888 Eastern South Lake Road, Changchun 130033, China
[d] Basic Experimental Center of Natural Science, University of Science and Technology Beijing, Beijing 100083, China

ARTICLE INFO

Article history:
Received 4 March 2022
Received in revised form 12 June 2022
Accepted 15 June 2022
Available online 17 June 2022

Keywords:
Broadband near-infrared
NIR pc-LED
Energy transfer
Garnet phosphor

ABSTRACT

Developing novel broadband near-infrared (NIR) phosphors is crucial to promote NIR phosphor-converted light emitting diodes (pc-LEDs) development. In this work, a new ultra-broadband NIR phosphor $Gd_3MgScGa_2SiO_{12}$: Cr^{3+} (GMSGS) was achieved by replacing Sc^{3+}-Ga^{3+} in $Gd_3Sc_2Ga_3O_{12}$ with Mg^{2+}-Si^{4+}. Under the excitation of blue light, the peak emission wavelength of GMSGS: $0.04Cr^{3+}$ is about 820 nm with a full width at half maximum (FWHM) of ~180 nm and an internal quantum efficiency (IQE) of 50 %. Benefited from the superposition of Cr^{3+} emission and highly efficient Yb^{3+} emission excited by energy transfer (ET) from Cr^{3+}, the codoped GMSGS: $0.04Cr^{3+}$, $0.007Yb^{3+}$ phosphor shows an ultra-broadband of 300 nm. Moreover, Yb^{3+}-codoping improves the thermal stability due to the ET from Cr^{3+} to more thermally stable Yb^{3+} emitters, and the integrated intensity of GMSGS: $0.04Cr^{3+}$, $0.007Yb^{3+}$ at 400 K was 63 % of that at room temperature. The packaging results exhibit that ~20 mW output power was achieved at 100 mA input current, which suggests promising potential of GMSGS: Cr^{3+}, Yb^{3+} phosphor in NIR pc-LED applications.

1. Introduction

Growing attention towards food safety and medical health is stimulating a huge market demand for smart wearable devices and portable optical devices with real-time monitoring capabilities [1–3]. The near-infrared (NIR) light covers a wavelength range of 650–1400 nm. It has the characteristics of large penetration depth and non-destructive in biological organisms, and can be applied to biomedical fields such as blood oxygen monitoring, biometric identification, vivo bioimaging [4–8]. LEDs have the advantages of small size, long lifetime and high luminous efficiency compared to conventional tungsten and halogen lamps [9–13]. Unfortunately, their narrow bandwidth (< 50 nm) is not sufficient to meet the broad-band emission requirements of NIR light sources. Inspired by the white LED, the NIR light source obtained from the NIR phosphor covered blue LED chip provides an idea to solve this problem [14–16]. The key is to explore new long-wave broadband NIR phosphors that can be effectively excited by blue LEDs.

Transition metal Cr^{3+}-doped inorganic phosphors emerge from the large number of rare earth doped phosphors due to its tunable broadband emission [17–19]. The emission spectra of Cr^{3+} ions are influenced by the crystal field environment, with a narrow band emission around 690 nm controlled by the spin forbidden ($^2E_g \rightarrow {}^4A_{2g}$) in the strong crystal field environment, and a broad band emission with the spin-allowed $^4T_{2g} \rightarrow {}^4A_{2g}$ transition in the weak crystal field environment [20,21]. By tuning the matrix crystal field, Cr^{3+}-doped materials can achieve broadband absorption and emission, which are the preferred materials for NIR luminescence [22,23]. The garnet structure has attracted much attention in the white LEDs phosphors for its excellent physicochemical properties [24,25]. For example, Lin et al. reported garnet phosphors $Ca_2YHf_2Al_3O_{12}$: Cr^{3+} with a peak wavelength of 775 nm and full-width at half maximum (FWHM) of 137 nm [26]. Jiang et al. reported $Y_3(MgAl)(Al_2Si)O_{12}$: $0.06Cr^{3+}$ phosphor with a peak wavelength of 760 nm and FWHM of 160 nm [27]. Basore et al. reported $Gd_3Sc_{1.47}Al_{0.5}Ga_3O_{12}$: $0.03Cr^{3+}$ phosphor with a peak wavelength of 756 nm and FWHM of 120 nm

* Corresponding author.
E-mail address: yjsu@ustb.edu.cn (Y. Su).

https://doi.org/10.1016/j.jallcom.2022.165912
0925-8388/

Table 1
Crystal field parameters and spectral parameters for Cr^{3+} in different garnet.

Phosphors	D_q (cm^{-1})	B (cm^{-1})	D_q/B	Wavelength (nm)	FWHM (nm)	IQE (%)	Reference
$Gd_3Sc_2Ga_3O_{12}$: Cr	1570	640	2.45	756	112	/	This work
$Gd_3ScMgGa_2SiO_{12}$: Cr	1550	685	2.26	820	180	50	This work
$Gd_3ScMgGa_2GeO_{12}$: Cr	1558	660	2.36	805	163	/	This work
$Gd_3Mg_2GaGe_2O_{12}$: Cr	1580	626	2.52	790	163	/	This work
$Ca_2LuScGa_2Ge_2O_{12}$: Cr	1460	741	1.97	800	150	/	[31]
$Ca_2YHf_2Al_3O_{12}$: Cr	1531	673	2.27	775	137	75	[26]
$Ca_2LaHf_2Al_3O_{12}$: Cr	1457	787	1.85	780	141	33	[30]
$Ca_2Lu_1Zr_2Al_3O_{12}$: Cr	1576	646	2.38	780	150	69	[29]
$Ca_2LuHf_2Al_3O_{12}$: Cr	/	/	/	785	148	/	[39]
$Y_2CaSiAl_4O_{12}$: Cr	1647	678	2.43	744	160	75.9	[21]
$La_3Sc_2Ga_3O_{12}$: Cr	1458	642	2.27	795	145	60	[32]

[28]. The co-doping of Cr^{3+}/Yb^{3+} has been demonstrated to be an effective strategy to further broaden the bandwidth due to the energy transfer from Cr^{3+} to Yb^{3+}. Zhang et al. reported $Ca_2LuZr_2Al_3O_{12}$: Cr^{3+}, Yb^{3+} phosphor with a peak wavelength of 780 nm and an IQE of 69.1 %. The bandwidth was extended from 150 nm to 320 nm after Cr^{3+}/Yb^{3+} co-doping [14,29]. Lin et al. reported $Ca_2LaHf_2Al_3O_{12}$:Cr^{3+} phosphor with a maximum peak located at 780 nm and an IQE of 33 %. The FWHM of the phosphor was extended from 141 nm to 300 nm after Cr^{3+}/Yb^{3+} co-doping [30].

As far as we know, almost all of the reported Cr^{3+} doped garnet NIR phosphors show emission wavelengths less than 800 nm and the full width at half maximum (FWHM) less than 160 nm , making it difficult to match the prepared pc-LEDs well with silicon-based photodetectors, some representative garnet phosphors that have been reported are listed in Table 1 [14,20,21,26,29–32]. Further research is needed to explore novel NIR phosphors with ultra-broadband and long emission wavelength. In this paper, a new ultra-broadband (FWHM = 180 nm) NIR $Gd_3MgScGa_2SiO_{12}$: Cr^{3+} (GMSGS) phosphor was achieved by replacing Sc^{3+}-Ga^{3+} in $Gd_3Sc_2Ga_3O_{12}$ with Mg^{2+}-Si^{4+}, with a peak wavelength of ~820 nm and a high IQE of ~50 %. After co-doping with Yb^{3+}, the bandwidth of the phosphor was extended from 180 nm to 300 nm. The effect of Mg^{2+}-Si^{4+}/Ge^{4+} substitution on the structure and luminescence properties was discussed, which illustrates that Cr^{3+} may enter two kinds of octahedral lattices to increase the FWHM, since the ionic radii of Mg^{2+} (0.72 Å) and Sc^{3+} (0.745 Å) are similar and larger than that of Cr^{3+} (0.615 Å). On the other hand, ion substitution weakens the crystal field according to the redshift of the emission spectra. The luminescence performance was analyzed based on energy transfer (ET). The packaging results exhibited that 20 mW output power was achieved at 100 mA input current.

2. Experimental

High-temperature solid-state method was used to prepare GMSGS: Cr^{3+}, Yb^{3+} phosphors. Gd_2O_3(99.99 %), Sc_2O_3(99.99 %), MgO (99.99 %), SiO_2(99.9 %), GeO_2(99.9 %), Ga_2O_3(99.99 %), Cr_2O_3(99.99 %), Yb_2O_3(99.99 %) were used as raw materials. Various raw materials were weighed according to stoichiometry. Mixing all raw materials thoroughly and sintering at 1400 °C for 6 h with reducing atmosphere 25 %H_2 + 75 %N_2. Finally, the naturally cooled phosphors were crushed and tested for analysis.

The phase structure properties were measured by X-ray diffractometer (Rigaku D/max-II B with Cu Ka radiation, operated at 40 kV and 20 mA). The diffraction pattern used for Rietveld analysis was collected in the same way. Rietveld refinement was performed by GSAS software. The excitation spectra, emission spectra, fluorescence lifetimes, temperature dependent properties, quantum efficiencies were all measured by an FLS-1000 fluorescence spectrophotometer. The morphology and element mappings of the as-prepared phosphors were measured with a field emission scanning electron microscope. The photoelectric properties of the LED were measured using a HAAS 2000 photoelectric measuring system (350–1100 nm, EVERFINE, China).

3. Results and discussion

3.1. Garnet-type structural properties

A series of $Gd_3Mg_mSc_{2-m}Ga_{3-m}Si_mO_{12}$: Cr^{3+} (m = 0, 0.5, 1.0, 1.5, 2) phosphors were prepared, and XRD patterns are displayed in Fig. 1**a**. The XRD pattern of the $Gd_3Sc_2Ga_3O_{12}$: Cr^{3+} (m = 0) corresponds well with the standard card (PDF#88–1199). With the increase of Mg^{2+}-Si^{4+} pair, XRD diffraction peaks shift to larger 2θ angles gradually due to the smaller ionic radius of Mg^{2+}-Si^{4+} (0.72–0.26 Å) pair than that of Sc^{3+}-Ga^{3+} (0.745–0.47 Å) pair, showed in right inset. When m = 2, the lattice distortion caused by the radius difference is too large and the hybrid phase appears, which is identified as SiO_2. A similar trend appears in the Mg^{2+}-Ge^{4+} substituted $Gd_3Mg_mSc_{2-m}Ga_{3-m}Ge_mO_{12}$: Cr^{3+}(m = 0, 0.5, 1.0, 1.5, 2) phosphors (Fig. 1b). The difference is attributed to that the radius of Ge^{4+} (0.39 Å) is similar to that of Ga^{3+} (0.47 Å), so the pure $Gd_3Mg_2Ga_1Ge_2O_{12}$: Cr^{3+} phase was obtained.

Fig. 2a exhibits the X-ray diffraction (XRD) patterns of $Gd_3MgScGa_2SiO_{12}$: xCr^{3+} (GMSGS) (x = 0.005–0.08). The XRD patterns of all samples correspond well with the standard card (PDF#85–0545), indicating that the prepared samples are pure garnet phase and the doping of Cr^{3+} didn't change the matrix crystal structure. With the increase of Cr^{3+} concentration, the XRD diffraction peak in 32–32.5° moves to a larger 2θ angle gradually (right

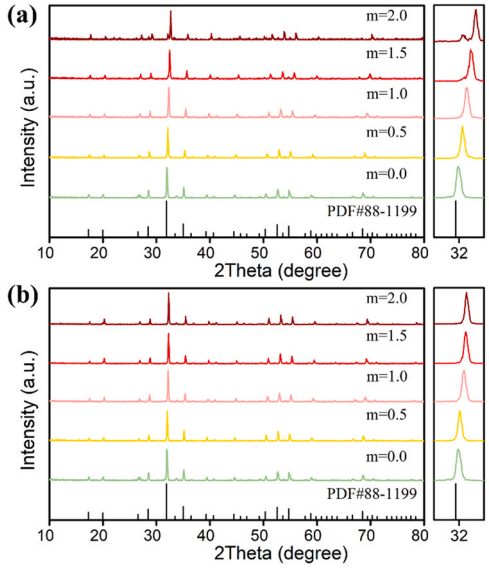

Fig. 1. XRD patterns of (a) $Gd_3Mg_mSc_{2-m}Ga_{3-m}Si_mO_{12}$: Cr^{3+} and (b) $Gd_3Mg_mSc_{2-m}Ga_{3-m}Ge_mO_{12}$: Cr^{3+} (m = 0, 0.5, 1.0, 1.5, 2). Right inset shows the XRD diffraction peak in 31–33°.

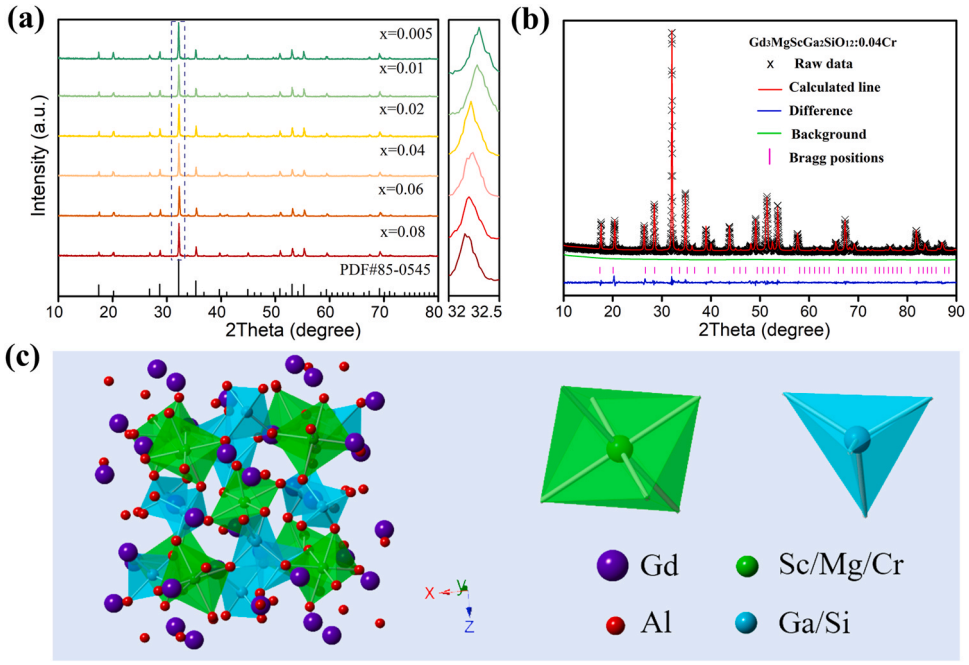

Fig. 2. XRD patterns and crystal structure diagram of GMSGS: Cr^{3+}. (a) XRD patterns of GMSGS: xCr^{3+} (x = 0.005, 0.01, 0.02, 0.04, 0.06, 0.08). Right inset shows the XRD diffraction peak in 32–32.5°. (b) Rietveld refinement XRD pattern of GMSGS: 0.04Cr^{3+}. (c) Crystal structure diagram of GMSGS: Cr^{3+}.

inset of Fig. 2a). According to the Bragg's equation $2dsin\theta = n\lambda$, the increase of the θ indicates the decrease of the lattice crystal plane spacing. The ionic radii of Cr^{3+}, Mg^{2+} and Sc^{3+} are 0.615 Å, 0.72 Å and 0.745 Å (CN=6, CN: Coordination Number) respectively. Since the Cr^{3+} ionic radius is smaller than that of Sc^{3+} and Mg^{2+} in octahedral, the lattice crystal plane spacing decreases and the XRD peak moves to a higher 2θ, which also proves that the Cr^{3+} ions have been successfully incorporated into the main lattice.

To obtain detailed crystal structure parameters, the Rietveld refinement of the GMSGS: 0.04Cr^{3+} was carried out, PDF#85–0545 was used as the initial model (Fig. 2b). The results show that the refinement converges to χ^2 = 1.64, R_{wp} = 12.9 %, and R_p = 9.5 %, respectively. The cell parameters are a = b = c = 12.4355 Å. These results indicate that Cr^{3+} successfully enters the lattice. GMSGS: Cr^{3+} belongs to the cubic crystal system with space group Ia $\bar{3}$d (No. 230), and the crystal structure diagram is shown in Fig. 2c. The octahedral structural unit is shown in green, and the tetrahedral structural unit is shown in blue. Mg^{2+}/Sc^{3+} and Si^{4+}/Ga^{3+} occupy the octahedral and tetrahedral lattice sites, respectively. Mg^{2+}/Sc^{3+} occupies the octahedral center and coordinates with six O^{2-} to form Mg^{2+}/Sc^{3+}-O^{2-} octahedra. Si^{4+}/Ga^{3+} occupies the tetrahedral center and coordinates with four O^{2-} to form Si^{4+}/Ga^{3+}-O^{2-} tetrahedra.

3.2. Morphology and element distribution

GMSGS: Cr^{3+} phosphor appears pale green under natural light. The SEM images of GMSGS: 0.04Cr^{3+} are shown in Fig. 3a, the phosphor particles are agglomerated and the diameter of one particle is about 5 μm. Fig. 3b shows the atomic ratios of GMSGS: 0.04Cr^{3+} phosphor, the atomic ratios of Gd, Mg, Sc, Ga, Si, O and Cr elements are 23: 4.46: 4.88: 8.59: 4.12: 54.61: 0.34, which are basically consistent with the design atomic ratio of 3: 1: 0.96: 2: 1: 12: 0.04. This indicates that the weighed raw materials all enter the design site. By comparing the element mapping in Fig. 3c, it can be seen that the elements are evenly distributed in the phosphor.

3.3. Ultra-broadband emission and energy transfer

Fig. 4a, b show the emission and excitation spectra of $Gd_3Mg_mSc_{2-m}Ga_{3-m}Si_mO_{12}$: 0.04$Cr^{3+}$ and $Gd_3Mg_mSc_{2-m}Ga_{3-m}Ge_mO_{12}$: 0.04$Cr^{3+}$ (m = 0, 0.5, 1.0, 1.5, 2). It can be seen from the figure that the excitation spectra contain two excitation bands located in the blue light region at ~450 nm and the red light region at ~650 nm, indicating that phosphors can be effectively excited by blue and red light. These two excitation bands correspond to the $^4A_{2g}\rightarrow{}^4T_{1g}$ and $^4A_{2g}\rightarrow{}^4T_{2g}$ transitions, respectively. Under blue light excitation, the emission spectra show near-infrared (700–1100 nm) broadband emission, which is attributed to the $^4T_{2g}\rightarrow{}^4A_{2g}$ transition of Cr^{3+} from the excited to the ground state. With increasing Mg^{2+}-Si^{4+} content (m), the peak emission wavelength of $Gd_3Mg_mSc_{2-m}Ga_{3-m}Si_mO_{12}$: 0.04$Cr^{3+}$ changes from 756 to 820 nm and the spectra blue shift from 820 to 792 when m changes from 1 to 2(Fig. 4d). The FWHM shows similar trend and reachs 180 nm when m= 1. As for $Gd_3Mg_mSc_{2-m}Ga_{3-m}Ge_mO_{12}$:0.04$Cr^{3+}$, the $Gd_3MgScGa_2GeO_{12}$: Cr^{3+} (GMSGG) also shows a broadband emission (FWHM = 163 nm) with a peak wavelength of ~805 nm. When the value of m continues to increase, the wavelength and FWHM remain essentially unchanged (Fig. 4e).

Fig. 4c shows the gaussian curve fitting of GMSGS: 0.04Cr^{3+}. The emission band can be divided into two emission peaks by gaussian fitting, with peak wavelengths of 11672.9 cm^{-1} (856.7 nm) and 12686.7 cm^{-1} (788.2 nm), respectively. This indicates that there are two luminescent centers in GMSGS. The luminescence of Cr^{3+} in the garnet structure always comes from the octahedral position. In GMSGS, Mg^{2+} and Sc^{3+} occupy the octahedral lattice position together. Considering that the radius of Cr^{3+} is similar to that of Mg^{2+} and Sc^{3+}, we believe that Cr^{3+} ions substitute the positions of Mg^{2+} and Sc^{3+} in the octahedron simultaneously [33]. It is shown that the overlapping of multiple luminescent centers emission bands can effectively broaden the emission bands [14,34,35].

The position of emission spectrum of Cr^{3+} is closely related to the crystal field environment, and the crystal field environment can be

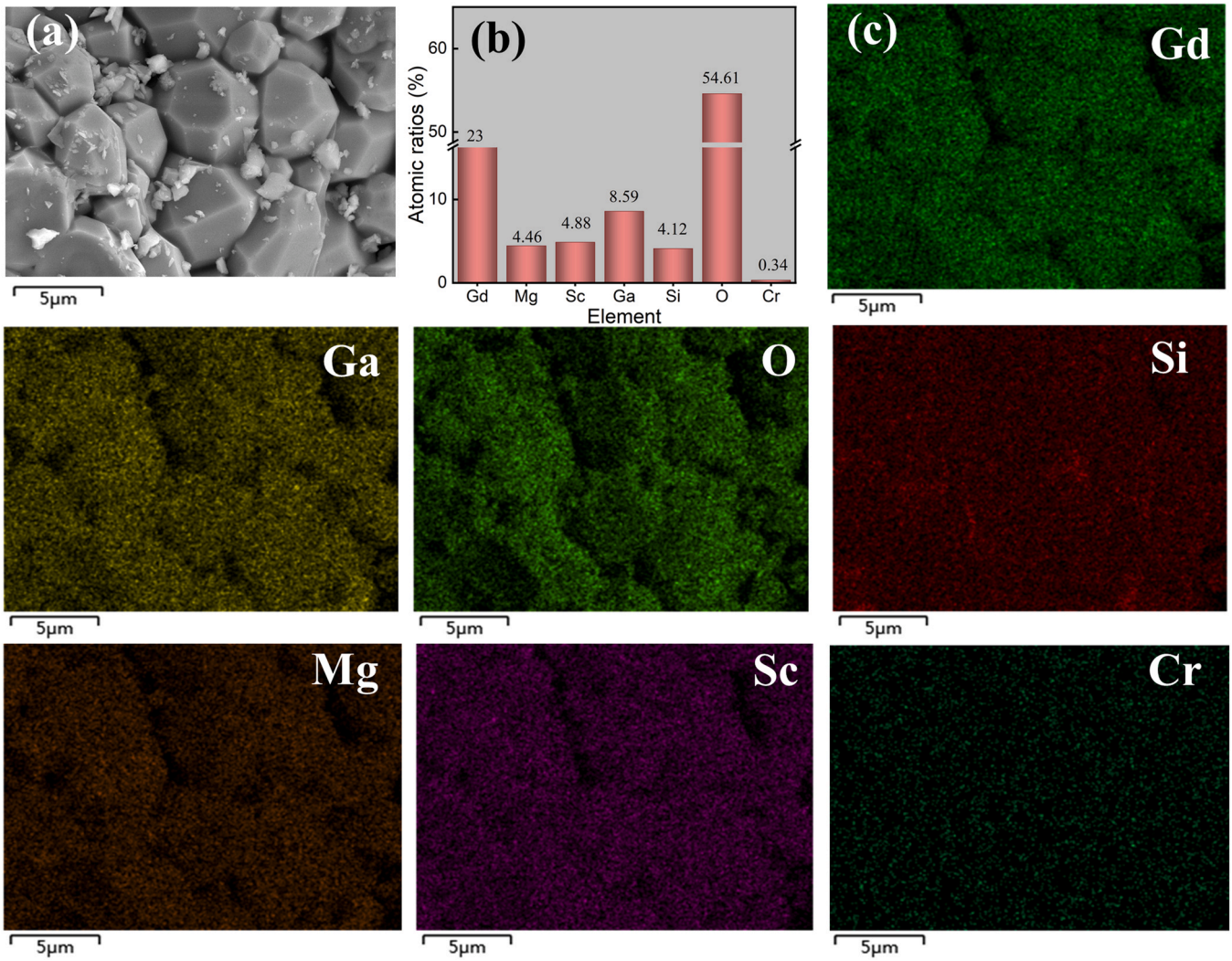

Fig. 3. The microstructure and elements distribution of GMSGS: $0.04Cr^{3+}$. (a) SEM image and (b) Atomic ratios of GMSGS: $0.04Cr^{3+}$. (c) EDS elemental mapping images of the GMSGS: $0.04Cr^{3+}$ sample.

estimated by the ratio of the octahedral crystal field parameter D_q to the Racah parameter B [36–38]. The crystal field parameters and spectral parameters of the reported garnet type broadband NIR phosphors are counted in Table 1. $Gd_3ScMgGa_2SiO_{12}$: $0.04Cr^{3+}$ in this work shows a weak crystal field environment, the longest emission wavelength and the largest FWHM.

Fig. 5a shows the emission spectra of GMSGS with different Cr^{3+} concentrations. With the increase of Cr^{3+} doping concentration, the peak wavelength of the emission spectra gradually shifts toward the long-wave direction. The increased reabsorption between Cr^{3+} due to the increase of Cr^{3+} concentration dominances the red-shift of the emission spectra [21,40]. Meanwhile, the luminescence intensity gradually increased with increasing Cr^{3+} concentration, and the intensity reached the maximum at x = 0.04, with an IQE of 50 %, followed by concentration quenching.

The interaction type between Cr^{3+} can be obtained by the Eq. (1):

$$I/x = \frac{K}{1 + \beta(x)^{\theta/3}} \quad (1)$$

where x is the doping concentration, I is the luminescence intensity of the sample at x doping concentration, K and β are constants under the same excitation conditions. $\theta = 3$ represents the energy transfer between the nearest neighbor ions, and $\theta = 6, 8, 10$ corresponds to the dipole-dipole, dipole-quadrupole and quadrupole–quadrupole interactions, respectively [41]. A plot of $\log(I/x)$ versus $\log(x)$ is given in Fig. 5b, and after a linear fitting, the slope of the line is −0.88 and $\theta = 2.64$, which is closest to 3. Accordingly, energy transfer between near-neighbor ions is the main concentration quenching mechanism for GMSGS: xCr^{3+}.

Due to the effect of energy transfer (ET) between Cr^{3+} and Yb^{3+}, the luminescence intensity of Cr^{3+} decreases with the increase of Yb^{3+} concentration. Fig. 6a gives a schematic diagram of Cr^{3+}/Yb^{3+} energy transfer, when Cr^{3+} is excited by 450 nm light, the $^4T_{1g}$ and $^4T_{2g}$ excited states returns to $^4A_{2g}$, showing broadband NIR emission at 820 nm. At the same time, Cr^{3+} in the excited state transfers energy to the $^2F_{5/2}$ energy level of Yb^{3+}, and when Yb^{3+} returns to the ground state, emitting narrow-band NIR light at 971 nm.

The emission spectra of GMSGS: $0.04Cr^{3+}$, yYb^{3+} with different Yb^{3+} concentrations are given in Fig. 6b. With the increase of Yb^{3+} doping concentration, the intensity of the Cr^{3+} keeps decreasing, while the intensity of the Yb^{3+} keeps increasing. Since the 450 nm excitation light cannot directly excite Yb^{3+} ions, ET can well tune the near-infrared intensity from Cr^{3+} to Yb^{3+} at 900–1100 nm. The co-doping of Yb^{3+} further increases the bandwidth of the GMSGS: $0.04Cr^{3+}$, $0.007Yb^{3+}$ emission spectrum to 300 nm. To investigate the ET process of $Cr^{3+} \rightarrow Yb^{3+}$, we measured the average lifetime of Cr^{3+} at different Yb^{3+} doping concentrations, and the decay curves are shown in Fig. 6c. The lifetime decay curves of Cr^{3+} can be well fitted

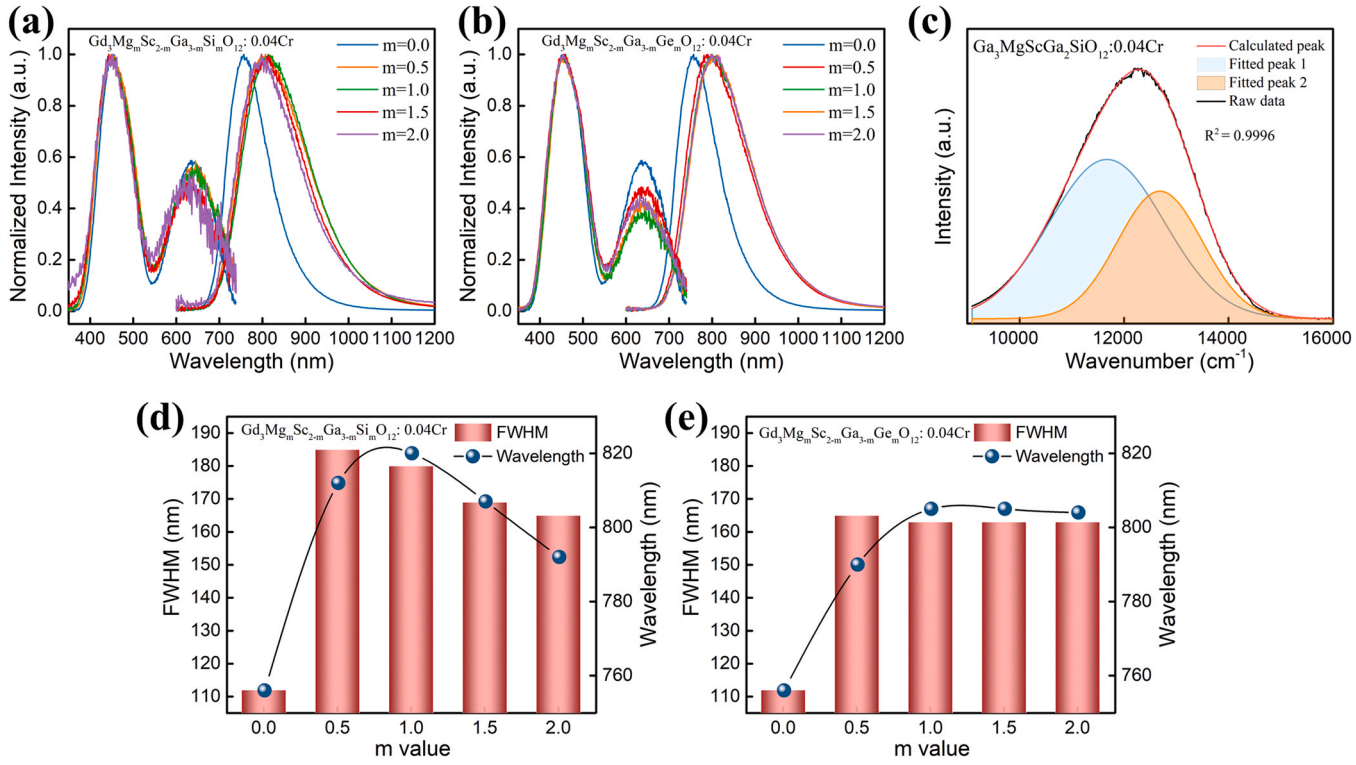

Fig. 4. Emission and excitation spectra of (a) $Gd_3Mg_mSc_{2-m}Ga_{3-m}Si_mO_{12}$: 0.04$Cr^{3+}$ and (b) $Gd_3Mg_mSc_{2-m}Ga_{3-m}Ge_mO_{12}$: 0.04$Cr^{3+}$ (m = 0, 0.5, 1.0, 1.5, 2). (c) Gaussian curve fittings of $Gd_3MgScGa_2SiO_{12}$: 0.04Cr^{3+}. The FWHM and peak wavelength of (d) $Gd_3Mg_mSc_{2-m}Ga_{3-m}Si_mO_{12}$: 0.04$Cr^{3+}$ and (e) $Gd_3Mg_mSc_{2-m}Ga_{3-m}Ge_mO_{12}$: 0.04$Cr^{3+}$ as a function of m values.

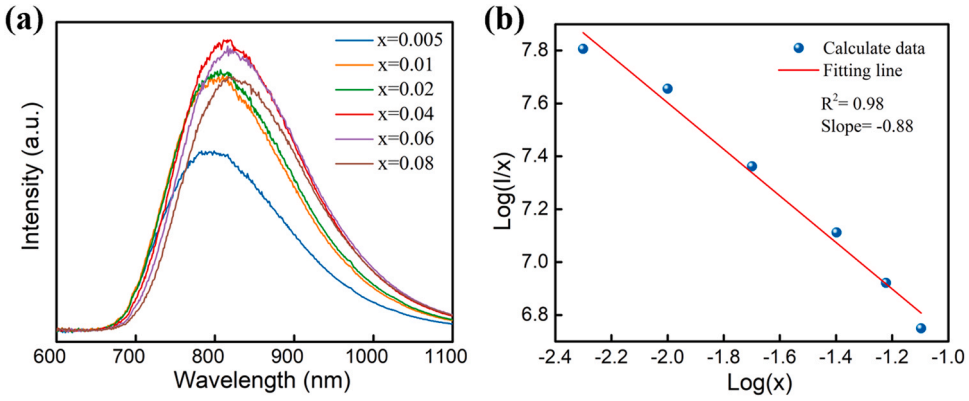

Fig. 5. The (a) emission spectra and (b) linear fitting of log (I/x) versus log (x) of GMSGS: xCr^{3+} (x = 0.005–0.08).

by the double exponential Eq. (2), which is consistent with the analysis on doual luminescence centers:

$$I(t) = B_1\exp(-t/\tau_1) + B_2\exp(-t/\tau_2) \quad (2)$$

where $I(t)$ is the real-time luminescence intensity of the sample, t is the time, B_1 and B_2 are the fitting constants, and τ_1 and τ_2 are the decay times of the fast and slow exponential components, respectively. The average lifetime (τ^*) can be calculated by Eq. (3):

$$\tau^* = \frac{B_1\tau_1^2 + B_2\tau_2^2}{B_1\tau_1 + B_2\tau_2} \quad (3)$$

The average lifetime of Cr^{3+} was calculated to decrease gradually with the increase of Yb^{3+} doping concentration, with $\tau = 51.7\mu s$ for y = 0 and $\tau = 45\mu s$ for y = 0.007.

The ET efficiency of $Cr^{3+}\rightarrow Yb^{3+}$ can be calculated according to Eq. (4) based on the decay time of Cr^{3+} [42].

$$\eta_{ET} = 1 - \frac{\tau}{\tau_0} \quad (4)$$

where η_{ET} is the ET efficiency, τ_0 is the decay time of single doped Cr^{3+}, and τ is the decay time after co-doping with different concentrations of Yb^{3+}. The ET efficiency of different concentrations of Yb^{3+} is shown in Fig. 6d, and the ET efficiency increases with the increase of y. η_{ET} = 12.9% for y = 0.007. Consequently, the co-doping of Yb^{3+} can broaden the emission spectrum due to the presence of ET.

3.4. Thermal quenching performance

The thermal stability of phosphors is a critical property for application to pc-LEDs due to the thermal accumulation of the device during operation. To investigate the thermal quenching properties of GMSGS: Cr^{3+}, Yb^{3+} phosphors, we measured the emission spectra of GMSGS: 0.04Cr^{3+}, GMSGS: 0.04Cr^{3+}, 0.003Yb^{3+} and GMSGS: 0.04Cr^{3+},

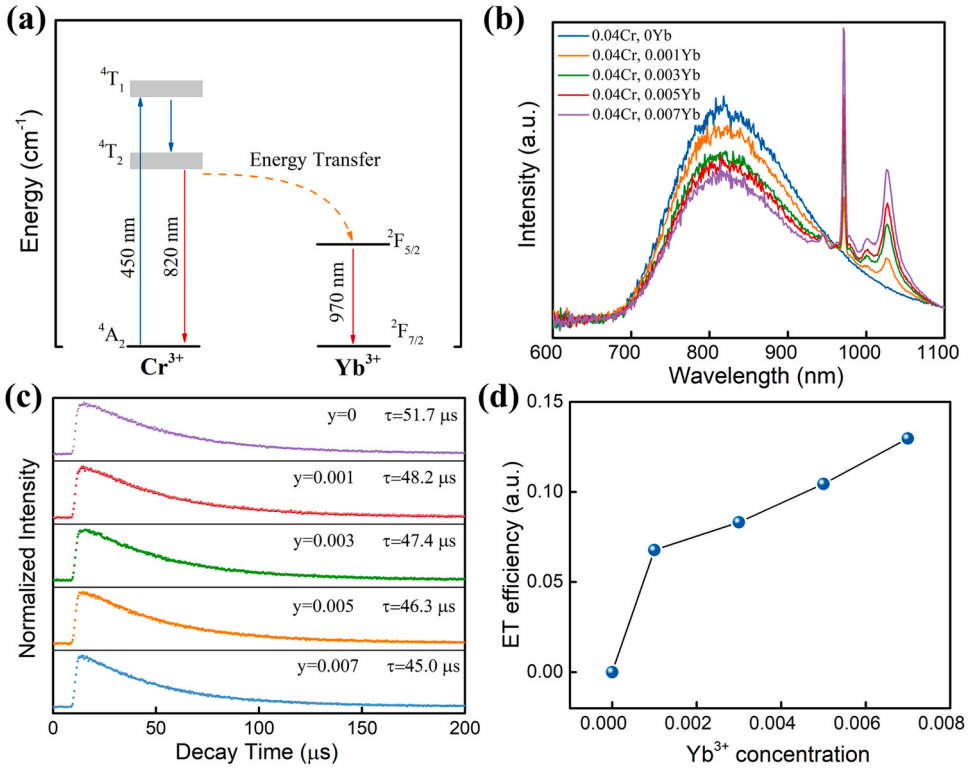

Fig. 6. Energy transfer properties of GMSGS: 0.04Cr^{3+}, yYb^{3+}. (a) Schematic diagram of Cr^{3+}/Yb^{3+} energy transfer. (b) Emission spectra. (c) Luminescent decay curves. (d) Energy transfer efficiency.

0.007Yb^{3+} phosphors at 80–500 K with a measurement interval of 30 K. The measurement results as shown in Fig. 7a~c.

As can be seen from the figure, the photoluminescence intensity of these samples decreases with increasing temperature due to the increase of non-radiative transitions. Notably, in the low temperature range (80–200 K), the emission spectra show a sharp R-line at 694 nm, and the intensity of the R-line gradually decreases until it disappears after the temperature continues to increase, which is

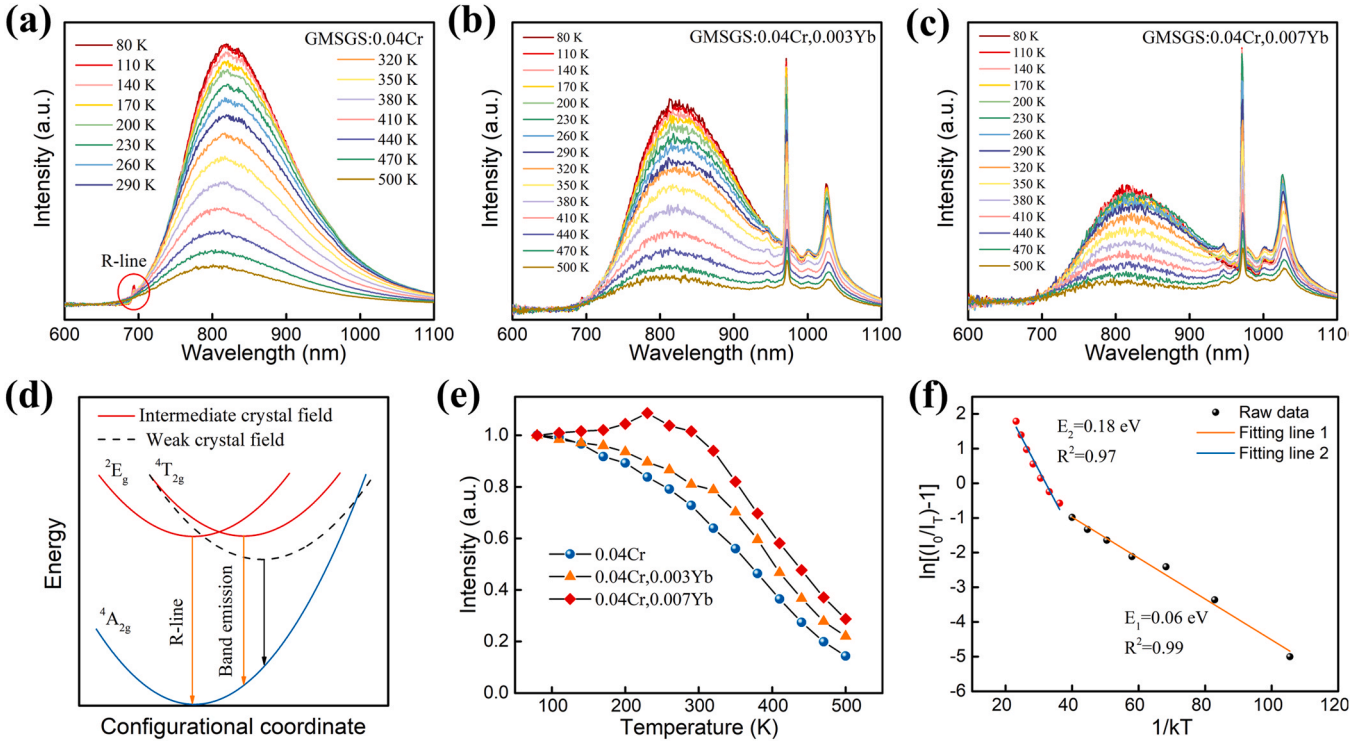

Fig. 7. Temperature dependent PL properties of GMSGS: Cr^{3+}, Yb^{3+} phosphors. (a) GMSGS: 0.04Cr^{3+}. (b) GMSGS: 0.04Cr^{3+}, 0.003Yb^{3+}. (c) GMSGS: 0.04Cr^{3+}, 0.007Yb^{3+}. (d) The schematic configurational coordinated diagram of intermediate crystal field. (e) Temperature dependence of the total emission intensity. (f) Linear fitting ln (I_0/I_T) versus 1/KT of the GMSGS: 0.04Cr^{3+} phosphor.

typical of Cr^{3+} intermediate crystal field emission [32,33,43]. The spectral shape is closely related to the Cr^{3+} crystal field strength. According to the Tanabe- Sugano energy level diagram [44,45], ^2E_g is the lowest excited state in the strong crystal field environment, while the transition of ^2E_g to the ground state $^4A_{2g}$ is spin-forbidden and shows sharp line emission. In the weak crystal field environment, $^4T_{2g}$ is the lowest excited state energy level, and the transition of $^4T_{2g}$ to the ground state $^4A_{2g}$ is spin-allowed, showing broad-band emission. Under low temperature conditions, Cr^{3+} is in a intermediate crystal field, resulting in the coexistence of R-line and broad-band emission [46,47], as shown in Fig. 7d.

Fig. 7e shows the total emission intensity of the three samples at different temperatures. The thermal stability of the samples gradually increases with the increase of Yb^{3+} concentrations. The emission intensity of GMSGS: $0.04Cr^{3+}$ decreases rapidly with increasing temperature under 450 nm excitation and decreases to 40 % when the temperature is heated to 400 K, which indicates a poor thermal stability. After codoping Yb^{3+}, the integrated intensity of GMSGS: $0.04Cr^{3+}$, $0.007Yb^{3+}$ phosphor at 400 K is about 63 % of the intensity at room temperature. This suggests that the thermal quenching of Cr^{3+} emission has a competitive relationship with the ET from Cr^{3+} to Yb^{3+} [48]. Due to the existence of both thermal quenching and energy transfer of Cr^{3+}, the thermal stability of Yb^{3+} is better than that of Cr^{3+}. When a closed Cr^{3+}-Yb^{3+} pair during energy transfer is formed, energy can be transferred to Yb^{3+} quickly and Cr^{3+} thermal quenching in the Cr^{3+}-Yb^{3+} pair is prevented. As a result, the thermal stability is enhanced [29,30,49]. Obviously, the introduction of Yb^{3+} greatly suppressed the thermal quenching behavior of GMSGS: $0.04Cr^{3+}$ phosphors, which is of great significance for the application of GMSGS: Cr^{3+}, Yb^{3+} phosphors in LEDs.

To further understand the thermal quenching properties of GMSGS: $0.04Cr^{3+}$ phosphor, we obtained the activation energy (ΔE) of the sample according to the Arrhenius equation.

$$I_T = \frac{I_0}{1 + Cexp(-\Delta E/kT)} \quad (5)$$

where I_T is the emission intensity of the sample at temperature T, I_0 is the initial emission intensity, k represents the Boltzmann constant (8.617×10^{-5} eV K^{-1}), and C is a constant. ΔE is the activation energy, which can be obtained by linearly fitting $\ln(I_0/I_T)$ with $1/KT$. Fig. 7f shows the linear fitting $\ln(I_0/I_T)$ versus $1/KT$. It can be seen that the scatter can be well fitted by two straight lines, located in the low temperature region and the high temperature region, respectively. This indicates that the low-temperature region and the high-temperature region have different thermal processes, and the slope of the straight line in the high-temperature region is much larger than that in the low-temperature region, i.e., the high-temperature region has a larger activation energy. The temperature-dependent intensity of the multiple thermal processes can be expressed by the Eq. (6).

$$I_T = \frac{I_0}{1 + c_1 \quad exp(-E_1/kT) + c_2 \quad exp(-E_2/kT)} \quad (6)$$

where E_1 is the activation energy of the low temperature process and E_2 is the activation energy of the high temperature process. The calculated activation energy of the low-temperature process of GMSGS: $0.04Cr^{3+}$ phosphor is 0.06 eV, which is lower than that of the high-temperature process (0.18 eV). The activation energy of the low-temperature process (E_1) is a thermal quenching phenomenon caused by a nonradiative transition at the intersection of the excited and ground states, while the high-temperature process (E_2) should be a thermal ionization process [14,31].

3.5. NIR-pc-LED applications

To assess the practical application value of GMSGS: Cr^{3+}, Yb^{3+} phosphors, we coated GMSGS: $0.04Cr^{3+}$ and GMSGS: $0.04Cr^{3+}$, $0.007Yb^{3+}$ phosphors on a 460 nm blue chip and prepared NIR-pc-LEDs. The electro-optical conversion efficiency of blue LED chip is 42.5 % at a forward bias current of 20 mA and a voltage of about 2.59 V. The electroluminescence spectra of GMSGS: $0.04Cr^{3+}$ and GMSGS: $0.04Cr^{3+}$, $0.007Yb^{3+}$ phosphors at a forward bias current of 100 mA and a voltage of about 2.6 V are shown in Fig. 8a and c, respectively.

The output power and electro-optical efficiency of NIR LED devices fabricated from GMSGS: $0.04Cr^{3+}$ and GMSGS: $0.04Cr^{3+}$, $0.007Yb^{3+}$ phosphors at different input power are given in Fig. 8b **and** d. The output power of NIR emission (700–1100 nm) increases with increasing current, indicating that the output power of NIR LED devices are relatively stable to current [17]. The output power of the NIR LEDs prepared by GMSGS: $0.04Cr^{3+}$ and GMSGS: $0.04Cr^{3+}$, $0.007Yb^{3+}$ was 20 mW and 19.5 mW, respectively, when the driving current was 100 mA. This is due to the improvement of the overall emission efficiency in the near infrared after co-doping of Yb^{3+}. Since Yb^{3+} has higher luminescence efficiency, the luminescence efficiency of phosphor will be significantly enhanced when co-doped with Yb^{3+}, which is a commonly used method to enhance the luminescence efficiency of Cr^{3+}-doped NIR phosphor [29,30,50]. The electro-optical conversion efficiencies of the NIR LED devices fabricated with GMSGS: $0.04Cr^{3+}$ and GMSGS: $0.04Cr^{3+}$, $0.007Yb^{3+}$ phosphors decreased with increasing current, and the electro-optical conversion efficiencies were 7.7 % and 7.52 %, respectively, when the driving current was 100 mA. The decline of efficiency is mainly due to the so-called “efficiency droop” of the LED chip under large driving current [28]. Considering that the prepared pc-LEDs show relatively long peak wavelengths (~820 nm) and extremely wide FHWH (180 nm) in the NIR spectral region, GMSGS: Cr^{3+}, Yb^{3+} phosphors have a promising application in NIR LEDs.

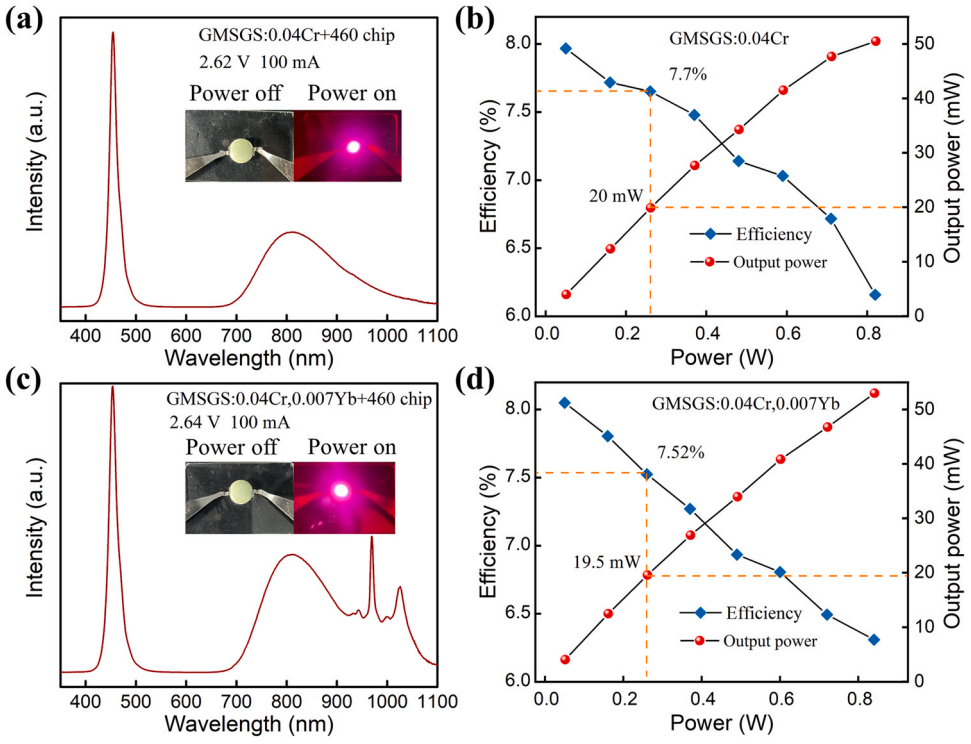

Fig. 8. Electroluminescence spectra of the NIR pc-LEDs fabricated by (a) GMSGS: 0.04Cr^{3+}, (c) GMSGS: 0.04Cr^{3+}, 0.007Yb^{3+} at 100 mA drive currents. The insets are the pc-LEDs and the lighted LED devices. The light output power and electro-optical efficiency of the NIR pc-LEDs fabricated by (b) GMSGS: 0.04Cr^{3+}, (d) GMSGS: 0.04Cr^{3+}, 0.007Yb^{3+} as a function of input power.

4. Conclusion

In summary, a series of $Gd_3Mg_mSc_{2-m}Ga_{3-m}Si_mO_{12}$: 0.04$Cr^{3+}$ and $Gd_3Mg_mSc_{2-m}Ga_{3-m}Ge_mO_{12}$: 0.04$Cr^{3+}$ (m = 0, 0.5, 1.0, 1.5, 2) broadband NIR phosphors were prepared by high-temperature solid-state method. By replacing Sc^{3+}-Ga^{3+} in $Gd_3Sc_2Ga_3O_{12}$ with Mg^{2+}-Si^{4+}, GMSGS: Cr^{3+} achieves a broadband emission centered at ~820 nm with a FWHM of ~180 nm. The GMSGS: 0.04Cr^{3+}, 0.007Yb^{3+} phosphors show bandwidth of 300 nm covering 700–1100 nm spectral range due to the superposition of Cr^{3+} and Yb^{3+} emission bands. The thermal stability was also improved notably, which was attributed to the suppression of thermal quenching by energy transfer. The output power of the NIR LEDs prepared by GMSGS: 0.04Cr^{3+}, 0.007Yb^{3+} shows 19.5 mW output power with 7.52 % electro-optical conversion efficiencies at 100 mA. The new developed GMSGS: Cr^{3+}, Yb^{3+} phosphors exhibit a promising potential in NIR pc-LED applications.

CRediT authorship contribution statement

Lipeng Jiang: Conceptualization, Data curation, Formal analysis, Investigation, Writing – original draft. **Xue Jiang:** Writing – review & editing. **Jihuan Xie:** Data curation, Formal analysis. **Haiying Sun:** Formal analysis. **Liangliang Zhang**: Writing – review & editing. **Xiuling Liu**: Formal analysis. **Zhaohui Bai**: Writing – review & editing. **Guocai Lv:** Formal analysis. **Yanjing Su:** Supervision, Writing – review & editing.

Declaration of Competing Interest

The authors declare that they have no known competing financial interests or personal relationships that could have appeared to influence the work reported in this paper.

Acknowledgements

This work was financially supported by the National Key Research and Development Program of China, China (2021YFB3501501), Guangdong Province Key Area R&D Program, China (2019B010940001).

References

[1] Y. Wang, Z. Wang, G. Wei, Y. Yang, S. He, J. Li, Y. Shi, R. Li, J. Zhang, P. Li, Ultra-broadband and high efficiency near-infrared $Gd_3Zn_xGa_{5-2x}Ge_xO_{12}:Cr^{3+}$ (x = 0–2.0) garnet phosphors via crystal field engineering, Chem. Eng. J. 437 (2022) 135346.
[2] Y. Yan, M. Shang, S. Huang, Y. Wang, Y. Sun, P. Dang, J. Lin, Photoluminescence properties of $AScSi_2O_6:Cr^{3+}$ (A = Na and Li) phosphors with high efficiency and thermal stability for near-infrared phosphor-converted light-emitting diode light sources, ACS Appl. Mater. Interfaces 14 (2022) 8179–8190.
[3] J. Lin, L. Zhou, L. Ren, Y. Shen, Y. Chen, J. Fu, L. Lei, R. Ye, D. Deng, S. Xu, Broadband near-infrared emitting $Sr_3Sc_4O_9$: Cr^{3+} phosphors: luminescence properties and application in light-emitting diodes, J. Alloy. Compd. 908 (2022) 164582.
[4] L. Cao, P. Li, J. Cui, X. Wang, Y. Yao, M. Zhang, M. Zheng, Z. Yang, H. Suo, Z. Wang, Achieving the potential multifunctional near-infrared materials $Ca_3In_{2-x}Ga_xGe_3O_{12}:Cr^{3+}$ using a solid state method, RSC Adv. 11 (2021) 10043–10053.
[5] D. Huang, H. Zhu, Z. Deng, H. Yang, J. Hu, S. Liang, D. Chen, E. Ma, W. Guo, A highly efficient and thermally stable broadband Cr^{3+}-activated double borate phosphor for near-infrared light-emitting diodes, J. Mater. Chem. C. 9 (2021) 164–172.
[6] M.T. Tran, D.Q. Trung, N. Tu, D.D. Anh, L.T.H. Thu, N.V. Du, N.V. Quang, N.T. Huyen, N.D.T. Kien, D.X. Viet, N.D. Hung, P.T. Huy, Single-phase far-red-emitting $ZnAl_2O^4:Cr^{3+}$ phosphor for application in plant growth LEDs, J. Alloy. Compd. 884 (2021) 161077.
[7] K. Omri, N. Alonizan, Effects of ZnO/Mn concentration on the micro-structure and optical properties of ZnO/Mn–TiO2 nano-composite for applications in photo-catalysis, J. Inorg. Organomet. Polym. Mater. 29 (2019) 203–212.
[8] C. Zhong, L. Zhang, Y. Xu, X. Wu, S. Yin, X. Zhang, H. You, Novel broadband near-infrared emitting phosphor $LiGe_2(PO_4)_3:Cr^{3+}$ with tuning and enhancement of NIR emission by codoping Sb^{5+}, J. Alloy. Compd. 903 (2022) 163945.
[9] C. Wang, X. Wang, Y. Zhou, S. Zhang, C. Li, D. Hu, L. Xu, H. Jiao, An ultra-broadband near-infrared Cr^{3+}-activated gallogermanate $Mg_3Ga_2GeO_8$ phosphor as light sources for food analysis, ACS Appl. Electron. Mater. 1 (2019) 1046–1053.
[10] H. Cai, H. Chen, H. Zhou, J. Zhao, Z. Song, Q.L. Liu, Controlling Cr^{3+}/Cr^{4+} concentration in single-phase host toward tailored super-broad near-infrared

luminescence for multifunctional applications, Mater. Today Chem. 22 (2021) 100555.
[11] K. Omri, A. Alyamani, L. El Mir, Surface morphology, microstructure and electrical properties of Ca-doped ZnO thin films, J. Mater. Sci.: Mater. Electron. 30 (2019) 16606–16612.
[12] D. Dai, Z. Wang, Z. Xing, X. Li, C. Liu, L. Zhang, Z. Yang, P. Li, Broad band emission near-infrared material $Mg_3Ga_2GeO_8$:Cr3+: Substitution of Ga-In, structural modification, luminescence property and application for high efficiency LED, J. Alloy. Compd. 806 (2019) 926–938.
[13] K. Omri, I. Najeh, L. El Mir, Influence of annealing temperature on the microstructure and dielectric properties of ZnO nanoparticles, Ceram. Int. 42 (2016) 8940–8948.
[14] L. Zhang, S. Zhang, Z. Hao, X. Zhang, G.-h Pan, Y. Luo, H. Wu, J. Zhang, A high efficiency broad-band near-infrared $Ca_2LuZr_2Al_3O_{12}$:Cr^{3+} garnet phosphor for blue LED chips, J. Mater. Chem. C. 6 (2018) 4967–4976.
[15] N. Mao, S. Liu, Z. Song, Y. Yu, Q. Liu, A broadband near-infrared phosphor $Ca_3Y_2Ge_3O_{12}$:Cr^{3+} with garnet structure, J. Alloy. Compd. 863 (2021) 158699.
[16] K. Omri, S. Gouadria, Dielectric investigation and effect of low copper doping on optical and morphology properties of ZO-Cu nanoparticles, J. Mater. Sci.: Mater. Electron. 32 (2021) 17021–17031.
[17] X. Xu, Q. Shao, L. Yao, Y. Dong, J. Jiang, Highly efficient and thermally stable Cr3+-activated silicate phosphors for broadband near-infrared LED applications, Chem. Eng. J. 383 (2020) 123108.
[18] D. Xu, Q. Zhang, X. Wu, W. Li, J. Meng, Synthesis, luminescence properties and energy transfer of Ca_2MgWO_6:Cr^{3+},Yb^{3+} phosphors, Mater. Res. Bull. 110 (2019) 135–140.
[19] S. Fang, T. Lang, M. Cai, T. Han, Light keys open locks of plant photoresponses: a review of phosphors for plant cultivation LEDs, J. Alloy. Compd. 902 (2022) 163825.
[20] L. Yao, Q. Shao, X. Xu, Y. Dong, C. Liang, J. He, J. Jiang, Broadband emission of single-phase $Ca_3Sc_2Si_3O_{12}$:Cr^{3+}/Ln^{3+} (Ln = Nd, Yb, Ce) phosphors for novel solid-state light sources with visible to near-infrared light output, Ceram. Int. 45 (2019) 14249–14255.
[21] M. Mao, T. Zhou, H. Zeng, L. Wang, F. Huang, X. Tang, R.-J. Xie, Broadband near-infrared (NIR) emission realized by the crystal-field engineering of $Y_{3-x}Ca_xAl_{5-x}Si_xO_{12}$:$Cr^{3+}$ (x = 0–2.0) garnet phosphors, J. Mater. Chem. C. 8 (2020) 1981–1988.
[22] S. Liu, Z. Wang, H. Cai, Z. Song, Q. Liu, Highly efficient near-infrared phosphor $LaMgGa_{11}O_{19}$:Cr^{3+}, Inorg. Chem. Front. 7 (2020) 1467–1473.
[23] F. Liu, W. Yan, Y.-J. Chuang, Z. Zhen, J. Xie, Z. Pan, Photostimulated near-infrared persistent luminescence as a new optical read-out from Cr^{3+}-doped $LiGa_5O_8$, Sci. Rep. 3 (2013) 1554.
[24] J. Ueda, S. Tanabe, INVITED) Review of luminescent properties of Ce^{3+}-doped garnet phosphors: New insight into the effect of crystal and electronic structure, Opt. Mater.: X 1 (2019) 100018.
[25] L. Jiang, X. Jiang, Y. Zhang, C. Wang, P. Liu, G. Lv, Y. Su, Multiobjective machine learning-assisted discovery of a novel cyan–green garnet: Ce phosphors with excellent thermal stability, ACS Appl. Mater. Interfaces 14 (2022) 15426–15436.
[26] Q. Zhang, G. Li, P. Dang, D. Liu, D. Huang, H. Lian, J. Lin, Enhancing and tuning broadband near-infrared (NIR) photoluminescence properties in Cr^{3+}-doped $Ca_2YHf_2Al_3O_{12}$ garnet phosphors via Ce^{3+}/Yb^{3+}-codoping for LED applications, J. Mater. Chem. C. 9 (2021) 4815–4824.
[27] L. Jiang, X. Jiang, J. Xie, T. Zheng, G. Lv, Y. Su, Structural induced tunable NIR luminescence of $(Y,Lu)_3(Mg,Al)_2(Al,Si)_3O_{12}$: Cr^{3+} phosphors, J. Lumin. 247 (2022) 118911.
[28] E.T. Basore, W. Xiao, X. Liu, J. Wu, J. Qiu, Broadband near-infrared garnet phosphors with near-unity internal quantum efficiency, Adv. Opt. Mater. 8 (2020) 2000296.
[29] S. He, L. Zhang, H. Wu, H. Wu, G. Pan, Z. Hao, X. Zhang, L. Zhang, H. Zhang, J. Zhang, Efficient super broadband NIR $Ca_2LuZr_2Al_3O_{12}$:Cr^{3+},Yb^{3+} garnet phosphor for pc-LED light source toward NIR spectroscopy applications, Adv. Opt. Mater. 8 (2020) 1901684.
[30] D. Huang, Q. Ouyang, H. Xiao, B. Wang, H. Lian, Q. Zeng, J. Lin, Cr,Yb-codoped $Ca_2LaHf_2Al_3O_{12}$ garnet phosphor: electronic structure, broadband NIR emission and energy transfer properties, Dalton Trans. 50 (2021) 908–916.
[31] B. Bai, P. Dang, D. Huang, H. Lian, J. Lin, Broadband near-infrared emitting $Ca_2LuScGa_2Ge_2O_{12}$:Cr^{3+} phosphors: luminescence properties and application in light-emitting diodes, Inorg. Chem. 59 (2020) 13481–13488.
[32] B. Malysa, A. Meijerink, T. Jüstel, Temperature dependent Cr^{3+} photoluminescence in garnets of the type $X_3Sc_2Ga_3O_{12}$ (X = Lu, Y, Gd, La), J. Lumin. 202 (2018) 523–531.
[33] H. Zeng, T. Zhou, L. Wang, R.-J. Xie, Two-Site occupation for exploring ultra-broadband near-infrared phosphor—double-perovskite La_2MgZrO_6:Cr^{3+}, Chem. Mater. 31 (2019) 5245–5253.
[34] S. Nargelas, Y. Talochka, A. Vaitkevičius, G. Dosovitskiy, O. Buzanov, A. Vasil'ev, T. Malinauskas, M. Korzhik, G. Tamulaitis, Influence of matrix composition and its fluctuations on excitation relaxation and emission spectrum of Ce ions in $(Gd_xY_{1-x})_3Al_2Ga_3O_{12}$:Ce scintillators, J. Lumin. 242 (2022) 118590.
[35] H. Przybylińska, C.-G. Ma, M.G. Brik, A. Kamińska, J. Szczepkowski, P. Sybilski, A. Wittlin, M. Berkowski, W. Jastrzębski, A. Suchocki, Evidence of multicenter structure of cerium ions in gadolinium gallium garnet crystals studied by infrared absorption spectroscopy, Phys. Rev. B 87 (2013) 045114.
[36] B. Bai, P. Dang, Z. Zhu, H. Lian, J. Lin, Broadband near-infrared emission of $La_3Ga_5GeO_{14}$:Tb^{3+},Cr^{3+} phosphors: energy transfer, persistent luminescence and application in NIR light-emitting diodes, J. Mater. Chem. C. 8 (2020) 11760–11770.
[37] K. Elzbieciak, A. Bednarkiewicz, L. Marciniak, Temperature sensitivity modulation through crystal field engineering in Ga3+ co-doped $Gd_3Al_{5-x}Ga_xO_{12}$:Cr^{3+}, Nd^{3+} nanothermometers, Sens. Actuators B: Chem. 269 (2018) 96–102.
[38] B. Struve, G. Huber, The effect of the crystal field strength on the optical spectra of Cr3+ in gallium garnet laser crystals, Appl. Phys. B 36 (1985) 195–201.
[39] L. Zhang, D. Wang, Z. Hao, X. Zhang, G.-h Pan, H. Wu, J. Zhang, Cr^{3+}-Doped Broadband NIR Garnet Phosphor with Enhanced Luminescence and its Application in NIR Spectroscopy, Adv. Opt. Mater. 7 (2019) 1900185.
[40] J. Wu, W. Zhuang, R. Liu, Y. Liu, T. Gao, C. Yan, M. Cao, J. Tian, X. Chen, Broadband near-infrared luminescence and energy transfer of Cr^{3+}, Ce^{3+} co-doped $Ca_2LuHf_2Al_3O_{12}$ phosphors, J. Rare Earths 39 (2021) 269–276.
[41] L. Jiang, X. Zhang, C. Wang, H. Tang, S. Zhu, Q. Li, X. Mi, L. Lu, Luminescence and energy transfer of Sm^{3+}-codoped $Y_{2.9}Al_{4.25}Ga_{0.75}O_{12}$:$Ce^{3+}_{0.1}$ phosphor, J. Mater. Sci.: Mater. Electron. 28 (2017) 18898–18902.
[42] W.-J. Yang, T.-M. Chen, White-light generation and energy transfer in $SrZn_2(PO_4)_2$:Eu,Mn phosphor for ultraviolet light-emitting diodes, Appl. Phys. Lett. 88 (2006) 101903.
[43] Y. Zhang, S. Miao, Y. Liang, C. Liang, D. Chen, X. Shan, K. Sun, X.-J. Wang, Blue LED-pumped intense short-wave infrared luminescence based on Cr^{3+}-Yb^{3+}-co-doped phosphors, Light.: Sci. Appl. 11 (2022) 136.
[44] Y. Tanabe, S. Sugano, On the absorption spectra of complex ions. I, J. Phys. Soc. Jpn. 9 (1954) 753–766.
[45] Y. Tanabe, S. Sugano, On the absorption spectra of complex ions, III the calculation of the crystalline field strength, J. Phys. Soc. Jpn. 11 (1956) 864–877.
[46] J. Zhou, Z. Xia, Synthesis and near-infrared luminescence of $La_3GaGe_5O_{16}$:Cr^{3+} phosphors, RSC Adv. 4 (2014) 46313–46318.
[47] G.N.A. De Guzman, M.-H. Fang, C.-H. Liang, Z. Bao, S.-F. Hu, R.-S. Liu, [INVITED] Near-infrared phosphors and their full potential: a review on practical applications and future perspectives, J. Lumin. 219 (2020) 116944.
[48] J. Xiang, J. Zheng, X. Zhao, X. Zhou, C. Chen, M. Jin, C. Guo, Synthesis of broadband NIR garnet phosphor $Ca_4ZrGe_3O_{12}$: Cr^{3+}, Yb^{3+} for NIR pc-LED applications, Mater. Chem. Front. 6 (2022) 440–449.
[49] F. Zhao, H. Cai, Z. Song, Q. Liu, Structural confinement toward controlling energy transfer path for enhancing near-infrared luminescence, Chem. Mater. 33 (2021) 8360–8366.
[50] H. Suo, Y. Wang, X. Zhao, X. Zhang, L. Li, K. Guan, W. Ding, P. Li, Z. Wang, F. Wang, Rapid nondestructive detection enabled by an ultra-broadband NIR pc-LED, Laser Photonics Rev. n/a (2022) 2200012.